http://dx.doi.org/10.21577/0103-5053.20190192

J. Braz. Chem. Soc., Vol. 31, No. 2, 381-393, 2020
Printed in Brazil - ©2020 Sociedade Brasileira de Química

Article

Experimental and Theoretical Study of $LiMn_2O_4$ Synthesized by the Solution Combustion Method Using Corn Starch as Fuel

José M. Siqueira Jr.,[a] *Carolina T. Machado,*[a] *Daniel S. G. Quattrociocchi,*[b] *Francisco M. S. Garrido,*[c] *Leonardo M. da Costa,*[b] *Eduardo A. Ponzio,*[a,d] *Glaucio B. Ferreira*[a,b] *and Jackson A. L. C. Resende*[e]

[a]*Departamento de Química Inorgânica, Instituto de Química, Universidade Federal Fluminense, Campus do Valonguinho, Outeiro de São João Batista, s/n, 24020-141 Niterói-RJ, Brazil*

[b]*Programa de Pós-Graduação em Química, Instituto de Química, Universidade Federal Fluminense, Campus do Valonguinho, Outeiro de São João Batista, s/n, 24020-141 Niterói-RJ, Brazil*

[c]*Instituto de Química, Universidade Federal do Rio de Janeiro, Avenida Athos da Silveira Ramos, No. 149, Bloco A, 6º andar, Centro de Tecnologia, 21941-909 Rio de Janeiro-RJ, Brazil*

[d]*Grupo de Eletroquímica e Eletroanalítica (G_2E), Instituto de Química, Universidade Federal Fluminense, Campus Valonguinho, 24020-141 Niterói-RJ, Brazil*

[e]*Programa de Pós-Graduação em Ciências dos Materiais, Universidade Federal do Mato Grosso, Campus Universitário do Araguaia, Instituto de Ciências Exatas e da Terra, Avenida Universitária No. 3500, 78698-000 Pontal do Araguaia-MT, Brazil*

Lithium manganese oxide, $LiMn_2O_4$, was synthesized in two temperature stages, where the first consisted by an ecofriendly solution combustion method at 300 °C. Finally, the as-burned powders were thermal treated at 500 and 700 °C. The structural and morphological changes were evaluated by the Rietveld method and density functional theory (DFT) calculations. The Rietveld refinement indicates obtaining the spinel cubic phase $LiMn_2O_4$ and a small amount of Mn_2O_3. The analyses by scanning electron microscopy (SEM) and transmission electron microscopy (TEM) show a porous microstructure composed of nano-sized crystallites for the sample treated at 500 °C. In cyclic voltammetry, it was possible to observe that the reduction-oxidation reaction is reversible due to the shape of voltammograms and the anodic and cathodic peaks of Mn ions. The theoretical calculations considered the experimental crystallographic parameters. The unit cell volume change was evaluated according to distinct amounts of lithium ions in the structure. The removal of the Li^+ cations from the oxides promotes a volume contraction. Therefore, it was possible to evaluate the participation of the Mn^{3+} ions in the frontier region between the valence and conduction bands. The density of states (DOS) calculation shows a predominant contribution of the O 2p and Mn 3d orbitals in the frontier orbitals.

Keywords: $LiMn_2O_4$, solution combustion method, Rietveld refinement, DFT, nanoparticles, lithium-ion batteries

Introduction

Since 1990 lithium-ion batteries have been extensively used in a wide range of electronic equipment, electric vehicles and energy storage devices.[1-5] When compared with traditional rechargeable systems, as Pb-acid and Ni-Cd, the lithium-ion batteries have smaller dimensions, less weight, increased energy density without the memory effect.[4] Additionally, these batteries have a good cycling performance and high voltage, providing larger energy amount.[5,6] The Li-ion batteries typically use a graphite-lithium composite (Li_xC_6) as anode, lithium oxides ($LiCoO_2$ or $LiMn_2O_4$) as cathode and a conducting electrolyte.[7]

Due to the importance in the world of these batteries, the components of the cells (electrolytes, anodes and cathodes) are still object of research to improve their

*e-mail: jmsiqueirajunior@id.uff.br

properties. However, most of the recent studies are concentrated in the development of the cathode material.[8,9] Although the $LiCoO_2$ cathode has an excellent chemical stability and high charge performance, it also has an expensive value and has less than one Li^+ ion *per* unit cell.[10] Thus, fewer expensive alternative cathode materials must be developed for the large scale power batteries or stationary energy storage. Among the different materials studied, the spinel $LiMn_2O_4$ of the $Fd\bar{3}m$ space group[9] stands out due to its low cost, low toxicity, easy preparation and safety properties.

The crystalline structure of $LiMn_2O_4$ as well as the shape and size of the crystallites and grains are correlated with its electrochemical features.[11-13] The spinel $LiMn_2O_4$ structure consists of compact cubic close packing composed by oxygen atoms that form 32 octahedral sites and 64 tetrahedral sites, as shown in Figure 1.[11] The Mn^{3+} and Mn^{4+} ions occupy the octahedral sites, whereas the Li^+ ion occupies the tetrahedral sites or the empty octahedral sites. The structure of this material presents tridimensional channels that favor the transport of Li^+ ions. These channels are formed by the connection of the 8a tetrahedral sites with the empty 16d octahedral sites. Additionally, the crystal structure also presents vacancies and interstices that allow the charge compensation through the oxidative state variation of the Mn cation.[11-16] These sites are important in the oxidation and reduction processes, due to the charge compensation of the Mn^{x+} cation (x = 3 or 4) in the channel. The Jahn-Teller effect, due to the insertion/removal lithium processes, is associated with low cycling current.[16] The insertion/removal process of the lithium ions from the 8a tetrahedral sites occurs in the 4 V (*vs*. Li/Li^+) region maintaining the cubic symmetry. However, in the 3 V region with the Li^+ cation insertion, the valence of the manganese is below 3.5, which allows a transition phase between the cubic $LiMn_2O_4$ and the tetragonal $Li_2Mn_2O_4$ due to the Jahn-Teller effect, limiting its use only to the 4 V region.[17-19]

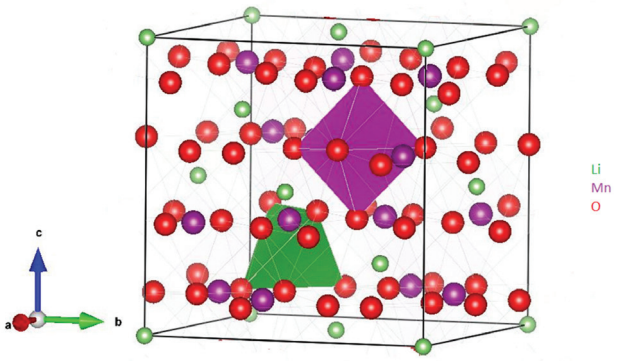

Figure 1. Crystalline structure of the spinel $LiMn_2O_4$ (Li, Mn and O atoms).

The synthetic preparation method of solids influences directly in the crystal aspects such as size, microstrain and crystallinity, which are important properties for the application in the electronic devices.[20] The lithium manganese oxide has been synthesized with different methods: co-precipitation,[21] hydrothermal,[22] sol-gel process with/without template,[23] synthesis by precursor[24] and solid-state reactions at high temperatures.[25] Naghash and Lee[21] obtained $LiMn_2O_4$ using the co-precipitation method where stearic acid was used to co-precipitate lithium and manganese. This product was calcinated in the air resulting in fine and homogenous particles of spinel $LiMn_2O_4$. Xu *et al*.[26] used the hydrothermal method to synthesize the $LiMn_2O_4$ doped with Co and Al. The spinel structure was not modified by the presence of the impure Co-Al and showed real gain in cycling stability and rate performance.[26] The solid state reaction is the most frequently used method for large-scale production in industry. It consists of the mixture of the solid precursors followed by high-temperature calcination, in a specific time amount, to obtain homogeneous and good quality samples. The cubic spinel $LiMn_2O_4$ is synthesized through lithium hydroxide, carbonate, or nitrate with manganese oxyhydroxide, carbonate or oxide and calcinated at high temperatures. This high temperature process can lead to solids with inhomogeneity, irregular morphology, larger particle size with broader particle size distribution and poor control of stoichiometry.[27-31] Recently, several studies in the literature[23,32,33] used the sol-gel combustion method to produce $LiMn_2O_4$. They produced $LiMn_2O_4$ at 650 and 800 °C using different fuels, ethylenediamine tetraacetic acid (EDTA) and citric acid, respectively. The gel formation allows the spinel phase synthesis at lower temperatures.[23]

In the present article, $LiMn_2O_4$ was synthesized using corn starch, an ecofriendly and low-cost fuel, in the solution combustion method. The synthesis was performed at 300 °C and the as-burned powder was calcinated at two distinct temperatures of 500 and 700 °C. The influence of the thermal treatment in morphology and microstructure was evaluated through X-ray powder diffraction (XRPD), scanning electron microscopy (SEM) and transmission electron microscopy (TEM) and Fourier transform infrared spectroscopy (FTIR). The influence of these materials characteristics in its electrochemical behavior was evaluated by cyclic voltammetry. Using theoretical calculations, the influence of the extraction of the Li^+ cation of the unit cell for the stoichiometry phase was studied. A density functional theory (DFT) study was performed to calculate electronic properties that were compared with experimental results.

Experimental

Reagents and materials

The compounds applied in this study were manganese(II) nitrate hexahydrate ($Mn(NO_3)_2.6H_2O$ Sigma-Aldrich, São Paulo, Brazil, ≥ 98%) and anhydrous lithium nitrate ($LiNO_3$, Vetec, Duque de Caxias, Brazil, 95%). The gel production was performed from starch (commercial corn starch, Maizena®, Duryea, Garanhuns, Brazil) in order to be an ecofriendly and low cost fuel.

Synthesis of $LiMn_2O_4$ using starch as complexing agent

Initially, a solution was prepared containing the proportion of Li:Mn = 1.1:2 using $LiNO_3$ (7.98×10^{-3} mol, 0.55 g) and $Mn(NO_3)_2.6H_2O$ (1.48×10^{-2} mol, 4.26 g), an excess of $LiNO_3$ was used to compensate Li losses during the synthesis.[9] Additionally, 1.0 g of starch was diluted in 10 mL of water and was added to each solution. The solution was agitated in an ultrasonic bath and was heated at 65 °C during 1 h until gel formation. The preparation of the crystalline powders were performed in two steps: firstly, with the combustion of the gels at 300 °C for 30 min and later the as-burned powder was thermal treated at 500 or 700 °C for 18 h, similar to that described in the literature.[34]

Material characterization

The infrared spectra were obtained using Nicolet FTIR 760 spectrometer. To perform this technique each sample was made into pellets with CsI and measured in the range from 4000-400 and 600-150 cm^{-1} wavenumber.

XRPD patterns were recorded using a 0.02° step and a 2 s acquisition time, in the range from 12 to 90° in 2θ with Synchrotron radiation source in the Brazilian Synchrotron Light Laboratory (LNLS, Campinas-SP, Brazil). The measurements were carried out in the "setup" mode of high intensity using pyrolytic graphite as crystal analyzer. The selected energy for the X-ray beam was 10.062 keV (λ = 1.2392 Å). Wavelengths and equipment zero points were obtained by the Rietveld refinement of several well-defined diffractions of LaB_6 (SRM660a) and Si (SRM 640c) standards.

Rietveld refinement

The Rietveld refinement was carried out applying the least squares method present in the GSAS software, EXPGUI version 1225 by Argonne National Laboratory.[35,36] The instrumental parameters were obtained by LaB_6 (SRM660a) standard sample. The average crystallite size for the samples was estimated using the Scherrer equation (equation 1), allowing the calculation of the crystallite size for each plane (*h k l*).

$$D = \frac{k\lambda}{\beta \cos\theta} \quad (1)$$

where λ = 1.2392 Å is the radiation wavelength, θ is the diffraction angle, k depends on crystal shape and reciprocal lattice point (k = 0.94),[37] β is the full width at half maximum (FWHM), D is the average crystallite size. The β term is described by the equation 2:

$$\beta = (\beta_e^2 - \beta_S^2)^{1/2} \quad (2)$$

where β_S and βe is the full width at half maximum of LaB_6 standard sample and sample, respectively. The microstructural analysis was performed from the results achieved after refinement with the GSAS software, which apply a microstrain distribution model, where the width of the diffraction peak increases according to the diffraction order. The GSAS software evaluates the crystallite size and microstrain analyzing the peak enlargement profile through mathematical routine. The function 4 (modified pseudo Voigt) of the GSAS program was used as it is more effective in the refinement of the desired profile, since it includes a model of anisotropic microstrain reported semi-empirically. This procedure was established by Stephens[38] and is not observed in other functions, only in function 4 of the GSAS software. The graphical representation of the three dimensional deformation distribution can be obtained using the refined data and a graphical support, MUSTRPLOT, present as routine of the GSAS program. This routine prepares a graphic file for displaying the effect of the Stephens microstrain model. The Williamson-Hall method[39] was also applied, trying to extraction of both contribution of microstrain and crystallite size in the full width at half maximum, simultaneously.

Electronic microscopy

The scanning electron microscopy (SEM) was obtained with JEOL JSM-7100F applying voltage of 15.0 kV where the compounds were deposited on double sided adhesive carbon tape on a metal support. The transmission electron microscopy (TEM) was obtained with JEOL JEM 2100F using voltage of 200.0 and 80.0 kV. These data allowed the evaluation of the morphology of the synthesized $LiMn_2O_4$ spinels.

Electrochemical measurements

The electrodes were prepared from a mixture of the lithium-manganese oxide nanoparticles (80 wt.%), black carbon (10 wt.%) and polyvinylidene fluoride (PVDF) (10 wt.%) in acetonitrile and immobilized on the gold electrode. After the materials immobilization, the gold electrode was polished with a 1200 sandpaper, alumina 1 μm, washed with distilled water and then dipped in acetonitrile to remove water. In a duly polished Au electrode, an aliquot of the dispersion containing nanoparticles was spread on the electrode. The solvent of that dispersion was evaporated for 40 min at 100 °C. This technique is widely diffused in the immobilization of nanoparticles.[40] The cells were assembled using 0.5 M $LiClO_4$ in acetonitrile as electrolyte, lithium-manganese oxide nanoparticles as working electrode, silver as pseudo-reference electrode and a stainless steel with large surface area as counter electrode. For the measurements, the potential was set in the range from −0.20 to 1.35 V *vs*. silver ($Ag|Ag^+$) as pseudo-reference electrode (2.80 to 4.35 V *vs*. $Li|Li^+$), and a scanning speed of 0.005 V s^{-1}. The electrochemical measurements were performed at room temperature using an Autolab potentiostat, μAutolab III model.

Computational details

The single point calculations in periodic boundary condition (PBC) were executed from the Rietveld refinement data. The DFT method through the exchange-correlation functional PBE-D3 (Perdew-Burke-Ernzerhof)[41,42] associated with generalized gradient approximation with the Hubbard U value (GGA+U) of Mn atoms in 4 eV, were applied in the software CP2K,[43] using the temperature of the system at 26.85 °C (300 K). The definition of the U parameter is chosen according to other Mn compounds reported in the literature[44-47] and was shown to be reasonable for a good prediction of the electronic structure of those Mn compounds. The results were obtained with mixed Gaussian and plane-wave method (GPW)[48-50] with valence double zeta (ζ) plus polarization, molecularly optimized, Goedecker-Teter-Hutter (DZVP-MOLOPT-GTH)[49] and Goedecker-Teter-Hutter pseudopotential (PBE-GTH).[50] The cut off density was 500 a.u. and the unit cell used in PBC was 1 × 1 × 1 ($a \times b \times c$ = unit cell parameters) containing $Li_8Mn_{16}O_{32}$. Additionally, from the structure obtained in Rietveld refinement, a single-point calculation was performed for the evaluation of the extraction of lithium ion of this structure. Also, for a more detailed analysis, the relaxation of the unit cell was carried out from the same methodology considering the samples with molar ratio 8:16, 6:16, 4:16 and 2:16 Li:Mn until the formation of the state with absence of lithium, which corresponds to the structure of MnO_2. The total ground state energy is converged within 1.0×10^{-5} eV *per* formula unit. All the calculations considered the presence of the Mn^{3+} and Mn^{4+} ions with the antiferromagnetic behavior[27] along the chain of Mn ions with alternating up and down spins in the (110) and (001) planes. Finally, density of states (DOS) calculations were performed for all the systems considering the population of each ionic specie, their respective frontier orbitals were also evaluated.

Results and Discussion

Synthesis

In the first step of the synthesis, the solution of manganese nitrate, lithium nitrate and corn starch was put in an ultrasound bath to obtain a homogeneous dispersion {complex ion $[Mn(H_2O)_6]^{2+}$ and the starch, $(C_6H_{10}O_5)_n$} and heated at 65 °C for a gel formation. The dilution effect of the gel on the ions prevents the growth of oxide particles, allowing the control of crystallite size.[51,52] In a second step, the gel was heated until 300 °C, leading to the as-burned powder. In this step the Mn^{2+} ion was oxidized by combustion atmosphere leading to the spinel $LiMn_2O_4$, as showed in equation 3. During this process the NO_2 gas was identified by the observation of a brown smoke.[51]

$$LiNO_{3(aq)} + 2Mn(NO_3)_{2(aq)} + \text{starch} \rightarrow LiMn_2O_{4(s)} + 5H_2O_{(g)} + 6CO_{2(g)} + 5NO_{2(g)} \quad (3)$$

In the third step the as-burned powder was thermal treated until 500 or 700 °C, each one for 18 h. This thermal treatment leads to particle growth, and larger crystallite sizes, with better homogeneity. The extent of this process is proportional to the temperature used, and aims to the process to reach equilibrium, at each temperature (500 or 700 °C). It is important to observe that the spinel $LiMn_2O_4$ was obtained at a lower temperature than through the traditional synthesis by solid state reaction (> 700 °C).[22,26-30] On the other hand, the synthesis was performed in three steps once the one-step procedure, at a higher temperature, is not suitable for the preparation of a porous structure since it favors sintering, which will be discussed later.[34]

Structural characterization

Infrared spectroscopy

Figure 2 shows the infrared spectrum of the gel obtained. In the gel spectrum the characteristic starch bands are observed. The bands in the region between 1500

and 1300 cm^{-1} are assigned to the angular deformations of H–C–H of starch and also to the nitrate ions from the precursors. The bands at 1153 and 1024 cm^{-1} refer to the axial deformation of C–O, of the ether and the alcohol of starch, respectively.[51] The bands that appear at 3390 and 1637 cm^{-1} are assigned to the O–H group of the water molecules. The first stretch mode is from the axial deformation of the O–H group and the second is assigned to the bending deformation mode.

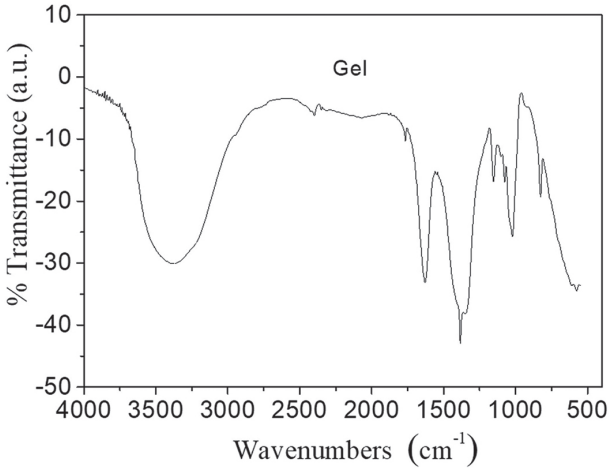

Figure 2. Infrared spectrum of the gel sample in CsI.

Figure 3 shows the infrared spectra of samples at different temperatures (300, 500 and 700 °C). In each temperature, we can observe the characteristic bands of the spinel $LiMn_2O_4$ around 615 and 510 cm^{-1}, which are assigned to the asymmetric stretching modes of the MnO_6 octahedron in the $LiMn_2O_4$ spinel structure.[23] The Mn–O stretching bands of sample treated at 700 °C are shifted, suggesting modifications in Mn–O binding for this sample. This behavior is probably related to a decrease in the Mn^{4+}/Mn^{3+} ratio in the spinel octahedral sites of this sample.[9,23] It is also possible to note that as the temperature increases, the bands assigned to the presence of organic residues between 1000-1500 cm^{-1} disappears due to the formation of CO_2 and water.

X-ray diffraction

A quantitative structural analysis of the 500 and 700 °C samples was evaluated through the Rietveld refinement. The analysis indicated the presence in all samples of $LiMn_2O_4$ as the major phase. The results also indicate the presence of a minor spurious phase of manganic oxide (Mn_2O_3). The refinement was performed from a high resolution synchrotron data, which allows the determination of the number of the crystalline phases and elucidate the X-ray diffraction patterns (Figures 4 and 5).[52]

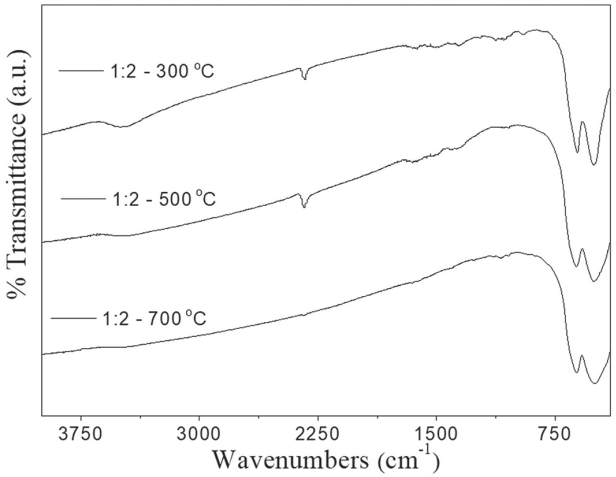

Figure 3. Infrared spectra in CsI of the samples treated at 300, 500 and 700 °C.

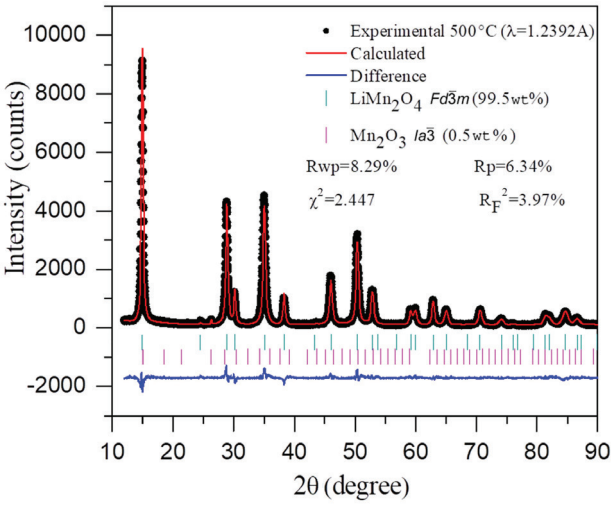

Figure 4. Experimental, calculated and the difference X-ray powder diffraction patterns for sample treated at 500 °C.

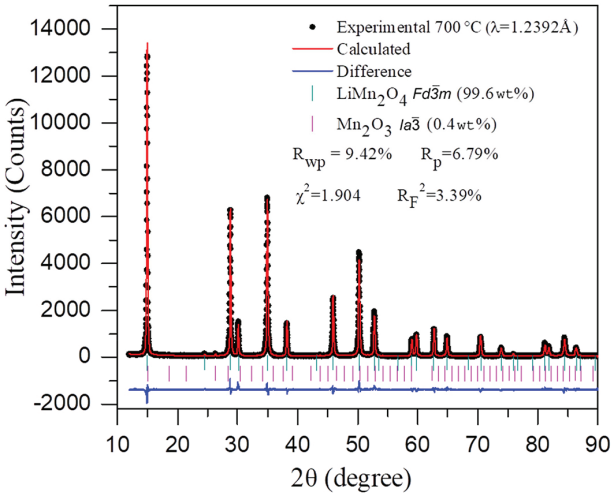

Figure 5. Experimental, calculated and the difference X-ray powder diffraction patterns for sample treated at 700 °C.

The analysis of Figures 4 and 5 shows that the difference among the adjustments made with the Rietveld refinement and the experimental pattern powder diffraction has good agreement. This is seen in both the Rietveld graphic and the figure of merit R_{wp} and χ^2. Each spinel solid was obtained with a 99.5 and 99.6 wt.% of the spinel cubic phase $LiMn_2O_4$ for the samples treated at 500 and 700 °C, respectively.

The Rietveld results adjusted from the output data of the GSAS software were used for microstructural analysis (crystallite size) and are listed in Table 1. There is an expansion of the lattice parameter of the $LiMn_2O_4$ with the 700 °C calcination temperature. This result can be explained considering a decrease in the Mn^{4+}/Mn^{3+} ratio, associated with a partial reallocation of Li^+ ions in the lattice sites.[53]

Table 1. Lattice parameter and crystallite size parallel (< t > //) and perpendicular (< t > ⊥) to anisotropic axis (001)

Calcination temperature / °C	Lattice parameter / Å	< t > // / nm	< t > ⊥ / nm
500	8.2248(1)	27(2)	20(2)
700	8.2413(1)	110(2)	48(2)

The analysis of Table 1 shows that the treated sample at 700 °C generates a larger crystallite size than at 500 °C. The crystallite obtained at 500 °C has smaller dimensions and a more square shape (27 × 20 nm). At 700 °C the crystallite size is almost a rectangle with the parallel and perpendicular dimensions four and two times larger (110 × 48 nm), respectively, than the treated sample at 500 °C.

Microstrain analysis

Scherrer equation is the simplest and most widely used method to estimate the average crystallite size from XRPD data. Thus, based on the FWHM values for the samples and for the LaB_6 standard, it was possible to calculate the average crystallite size values for some families of crystallographic planes as shown in Table 2. The analysis of Table 2 shows that the sample obtained at 700 °C is more homogeneous and its crystallite size is equal for the distinct crystallographic planes. In the sample treated at 500 °C, the crystallite size is not homogenous with large variations in the distinct crystallographic planes, varying from 23 nm in the (440) plane until 55 nm in the (111) plane. This result indicates a preferential crystallite growth for this sample.

The Scherrer equation gives us a rough estimate of average crystallite size. Despite the well-known accuracy of this method, it has the limitation that microstrain

Table 2. Crystallite size, obtained through Scherrer equation, for some families of crystallographic planes

Temperature / °C	Crystallite size / nm				
	Families of crystallographic planes / *hkl*				
	(111)	(311)	(400)	(511)	(440)
500	55(2)	41(1)	34(1)	26(1)	23(1)
700	40(1)	40(1)	40(1)	41(1)	41(1)

contribution to line broadening is not taken into account and the entire line broadening is assumed to result from small crystallite size.[54] A simple method to separate the contributions of particle size and microstrain of the line broadening in the XRPD patterns is the Williamson-Hall (WH) analysis. The method consists of a linear fit correlation of $\beta\cos\theta$ and $\sin\theta$ to analyze the crystallite size and the microstrain by equation 4.

$$\beta\cos\theta = \frac{k\lambda}{D} + 4\varepsilon\sin\theta \quad (4)$$

β is the peak diffraction corrected with LaB_6 (equation 2); D is the average crystallite size and ε is the microstrain in the sample which is assumed to be same in all crystallographic directions. This analysis supposes that crystallite size (D) and microstrain (ε) contribute independently of each other and are additive to the line broadening with Lorentzian profiles.

In this work, isotropic Williamson-Hall method referred to as uniform deformation model (UDM) was applied, as shown in Figure S1 of the Supplementary Information (SI) section. However, the Williamson-Hall analysis provides physically meaningless results for the system evaluated in this study. Other methods that incorporate the anisotropic nature of the crystal could be applied in order to extract this desired information,[55] but this is beyond the scope of this work. Thus, the influence of the microstrain was evaluated qualitatively applying the data of the Rietveld refinement and the results are presented in Figure 6.

The results indicate that the sample treated at 500 °C presents a greater influence of microstrain than the sample treated at 700 °C, where this was evidenced by analyzing the scale of three-dimensional axes in Figure 6.

Molecular modeling

The $LiMn_2O_4$ compound can present different crystalline arrangements, the cubic as obtained experimentally in this study, the tetragonal phase formed in temperature below 6.85 °C and another orthorhombic at −43.15 °C. In the

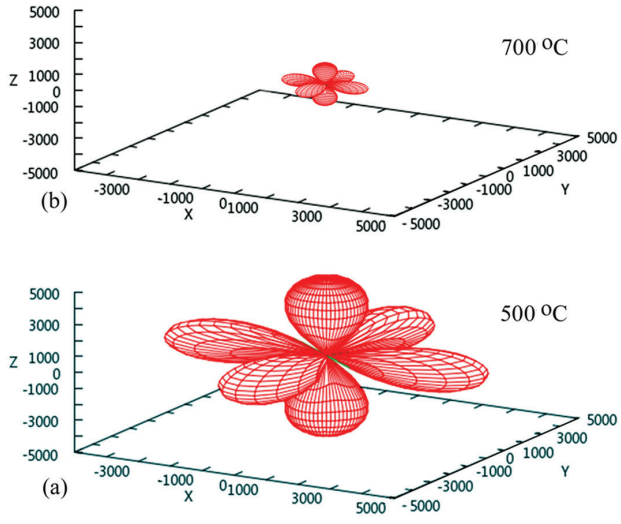

Figure 6. 3D plot of microstrain distribution for samples treated at (a) 500 and (b) 700 °C.

present article, due to the similarity of the crystallographic parameters obtained for $LiMn_2O_4$ spinel, we used as a starting point in our evaluation, the experimental data refined in 500 °C. Also, the $LiMn_2O_4$ unit cell was relaxed, resulting in an orthorhombic phase that is compatible with other studies reported in the literature.[56] To evaluate the crystalline parameters change with the lithium extraction of the tetrahedral sites of $LiMn_2O_4$, systems with different lithium contents were proposed until its total absence, which is equivalent to the formation of MnO_2. The results are summarized in Table 3.

The relaxed structures, obtained with different proportions of lithium ions, present lattice parameters indicating orthorhombic cells. However, the use of constrained cubic $LiMn_2O_4$ structure at room temperature does not give adequate prediction of the properties as a disorder function of the expected Mn^{3+}/Mn^{4+} arrangement, since DFT calculation does not predict even the Mn oxidation state ($Mn^{3.5+}$).[27] The MnO_2 structure was used to estimate the formation process of species containing only Mn^{4+} ions. This structure was also simulated as an orthorhombic structure and not as a cubic model. The difference of the lattice constant between the calculated and the experimental value is about 1%. The *a*/*b* of $LiMn_2O_4$ lattice predicted from GGA+U is smaller than the refined experimental value in this article (0.003 Å/0.017 Å). The *c*-axis lattice parameter of $LiMn_2O_4$ obtained from GGA+U is 8.30409 Å, which is about 0.06 Å larger than the experimental value.

The elongated *c*-axis is related mainly to the Mn–O bond expansion along the *z*-axis direction due to the Jahn-Teller (JT) distortion. The mean values of the Mn–O bonds of the octahedral MnO_6 sites, considering the oxidation states Mn^{3+} and Mn^{4+}, were compatible with the experimental values of 2.01 and 1.91 Å, respectively.[56] It is evident that the Jahn-Teller distortion is identified in these octahedral sites due to the larger fluctuation of the calculated bonds (± 0.0897 and ± 0.0317 Å) compared to the MnO_2 system constituted only by Mn^{4+} ions (± 0.0037 Å) with more symmetrical Mn–O bonds.

The results of lithium extraction on the $LiMn_2O_4$ structure was identified both in the continuous reduction of the unit cell volume as in most *a*/*b*/*c* lattice parameters. However, the values of *c* for the extraction from 4 lithium ions indicates a slightly positive oscillation, and volume contraction was caused by the variation of the *a*/*b* parameters. These structural variations were followed by a small change of the Li–O bonds at the tetrahedral sites with a mean reduction of 0.0076 Å and with an asymmetry of the bonds with a mean range of ± 0.0305 Å.

The evaluation of the fundamental magnetic state to $LiMn_2O_4$ and its delithiated state until-MnO_2 resulted into

Table 3. Band gap, Mn valence state, spin moment, unit-cell volume, *a*, *b*, *c* lattice parameters and Mn^{4+}–O, Mn^{3+}–O and Li–O distances

Structure	Optimized						Refined
	$Mn_{16}O_{32}$	$Li_2Mn_{16}O_{32}$	$Li_4Mn_{16}O_{32}$	$Li_6Mn_{16}O_{32}$	$Li_7Mn_{16}O_{32}$	$Li_8Mn_{16}O_{32}$	$Li_8Mn_{16}O_{32}$
Band gap / eV	2.27	1.33	1.10-1.33	1.24-1.50	1.16-1.41	1.03-1.45	0.38-0.74
Mn valence state	4+	4+/3+	4+/3+	4+/3+	4+/3+	4+/3+	3.5+
Spin moment	±3.2	±3.2/±4.0	±3.2/±4.0	±3.2/±4.0	±3.2/±4.0	±3.2/±4.0	±3.7
Unit-cell volume / Å^3	526.60840	537.76600	547.68557	556.68982	559.23755	562.03475	559.13105
a / Å	8.05260	8.11543	8.13921	8.20903	8.20005	8.23519	8.23831
b / Å	8.04672	8.08070	8.09816	8.20868	8.18227	8.21859	8.23831
c / Å	8.12705	8.20036	8.30927	8.26129	8.33502	8.30409	8.23831
Mn^{4+}–O / Å	1.9144 ± 0.0037	1.9158 ± 0.0224	1.9185 ± 0.0346	1.9183 ± 0.0275	1.9174 ± 0.0351	1.9197 ± 0.0391	1.9739 ± 0.0000
Mn^{3+}–O / Å	–	2.0155 ± 0.0887	2.0167 ± 0.0916	2.0165 ± 0.0925	2.0167 ± 0.0916	2.0138 ± 0.0841	1.9739 ± 0.0000
Li–O / Å	–	1.9418 ± 0.0286	1.9512 ± 0.0266	1.9622 ± 0.0255	1.9718 ± 0.0358	1.9723 ± 0.0358	1.9392 ± 0.0000

anti ferromagnetic states (AFM). Thus, in the definition of the appropriate bulk model of those systems the process of lithium ion extraction and variation of the manganese ions oxidation of Mn^{3+} (d^4:$t_2^3e^1$) to Mn^{4+} (d^3:$t_2^3e^0$) were evaluated.[27] This model was used as reference for the magnetic arrangement indicated in Figure 7 using the broken symmetry methodology for the correct indication of the spin states.

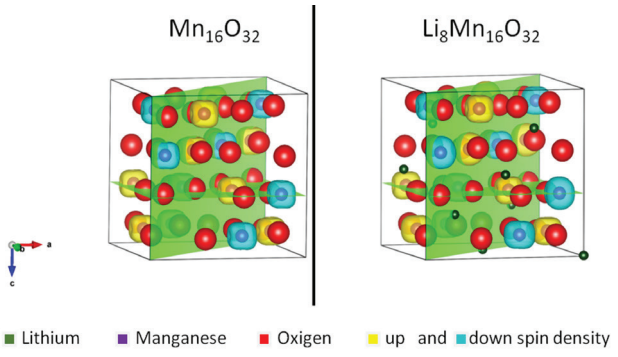

Figure 7. Spin moment in optimized structure of MnO_2 and $LiMn_2O_4$, with indication of planes (110) and (001) in green.

The evaluation of the electronic structure of these solids was performed from the density of states (DOS) analysis as presented in Figure 8, which the $LiMn_2O_4$ and MnO_2 relaxed structures were compared using periodic calculations. The other DOS graphs are found in the Figures S2-S8 (SI section) for a more complete evaluation. The results, performed with the GGA-PBE-D3+U functional, of the $Li_{8-x}Mn_{16}O_{32}$ (x = 8, 6, 4, 2, 1, 0) structures indicated a band gap of around 2.27 and 1.03 eV for calculated systems. These values are compatible with the literature.[57] However, considering the cubic structure experimentally refined for $LiMn_2O_4$, the band gap calculation presented a value of 0.38 eV. This variation can be rationalized by the absence of relaxation of the octahedral sites of the cubic structure.

The density of electronic states for the $LiMn_2O_4$ and MnO_2 compounds with relaxed structures show the Fermi energy (E_f) as the reference energy in zero. The valence band (VB) is presented between 0 and −1.5 eV, with values near the E_f. VB consists mainly by O 2p orbitals with small participation of the close energy Mn 3d orbitals. In contrast, values above the E_f make up the conduction band (CB) in the range from 0 to 1.0 eV, with a more detached hybridization for the Mn 3d orbitals and with small participation of O 2p orbitals. Another relevant observation obtained by the extraction of Li ions from the $LiMn_2O_4$ structure was the identification of occupied orbitals in a range from approximately 0.3 to 0.4 eV with strong participation of 3d orbitals of Mn^{3+} ions. The number

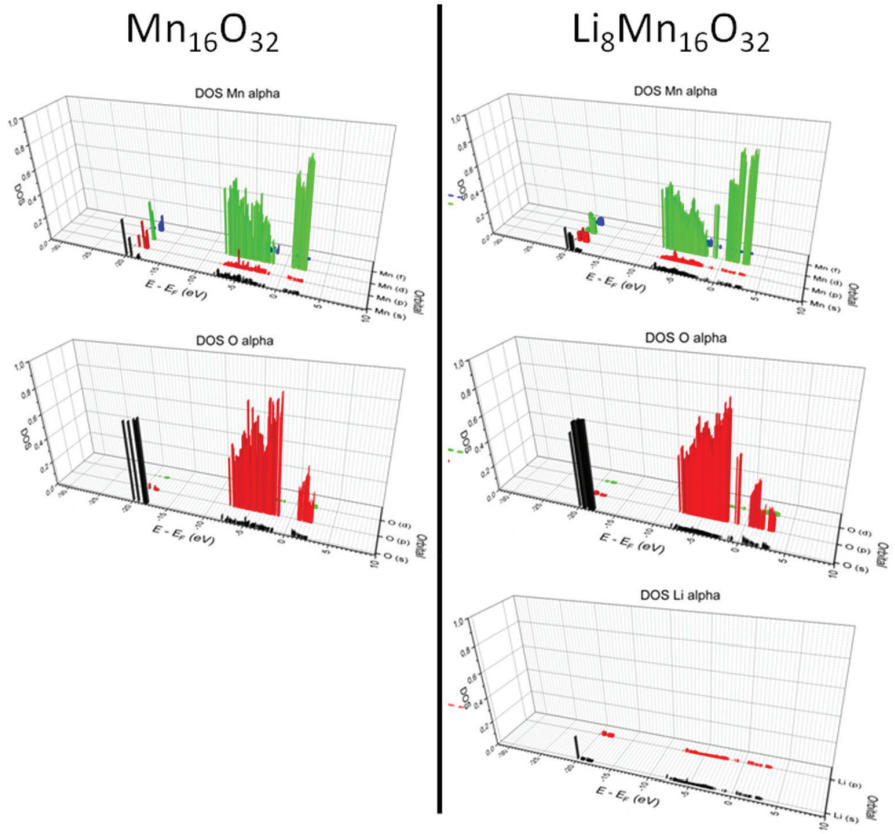

Figure 8. Density orbital state in optimized structure of MnO_2 and $LiMn_2O_4$.

of orbitals in this region was gradually reduced until the total removal of lithium ions and a constant increase of the theoretical band gap.

This behavior allows the correlation of the electronic structure with the redox process caused by the extraction of the lithium ions. This process of larger mobility of the lithium ions can be rationalized by the small participation of the Li orbital in the DOS for the regions close and around the E_f. This observation is also presented in Figure 9 where the highest occupied molecular orbital (HOMO) and lowest unoccupied molecular orbital (LUMO) are presented and it is possible to note the electronic density around the Mn and O ions and its absence around the Li ions. The overlap between the Li and O orbitals is not detached. Thus, due to their larger mobility, Li ions can be added and removed from the $LiMn_2O_4$ channel structure. This assists in achieving the charge and discharge electrochemical cycles when this compound is applied as a cathode in Li-ion batteries.[18]

The DOS, in Figure 9, present a predominant participation of the O 2p and Mn 3d orbitals in the HOMO/LUMO frontier orbitals and a small participation of the hybridization between these orbitals for $LiMn_2O_4$. The boundary orbitals in the $LiMn_2O_4$ have more localized density for the Mn^{3+} ions and the coordinating oxygen atoms. These results are distinct than the one found in other systems such as $LiCoO_2$,[10] which presents a homogeneous distribution of electron density by these atomic types. This is evidenced by the comparison of the frontier orbitals of MnO_2 that presents its distinct characteristic with the HOMO mainly populated by O 2p orbitals and LUMO by the d orbitals of the Mn^{4+} ion. In the Supplementary Information the distribution of molecular orbitals is shown in more details in Figure S9.

Electronic microscopy

The analyses by SEM show the morphology and texture of the $LiMn_2O_4$ synthesized with the starch precursor, as observed in Figures 10 and S10 (SI section), where the latter presents an evaluation by histograms. It can be observed in the SEM of the sample treated at 500 °C that a porous microstructure composed of nano-sized crystallites was formed. This morphology with several pores results from the combustion methodology used in the production of the solid, where gas elimination occurs. Particle aggregates without homogeneous morphology are generated in the combustion process. The beginning of a sintering process is also observed. The sample obtained after the heat treatment at 700 °C is also presented as an aggregate of crystallites. However, it does not present the same porosity texture of the sample treated at 500 °C, but a more pronounced sintering process, showing some particles with octahedral prismatic morphology.

The analyses by TEM (Figure 11) show that the sample treated at 500 °C presents the plane of atoms resulting from the alignment of the plane related to the Miller index (111) with a distance of 0.47 nm (compatible with the data of XRPD).[58] The average particle size around 14 nm with octahedral prismatic morphology is observed.

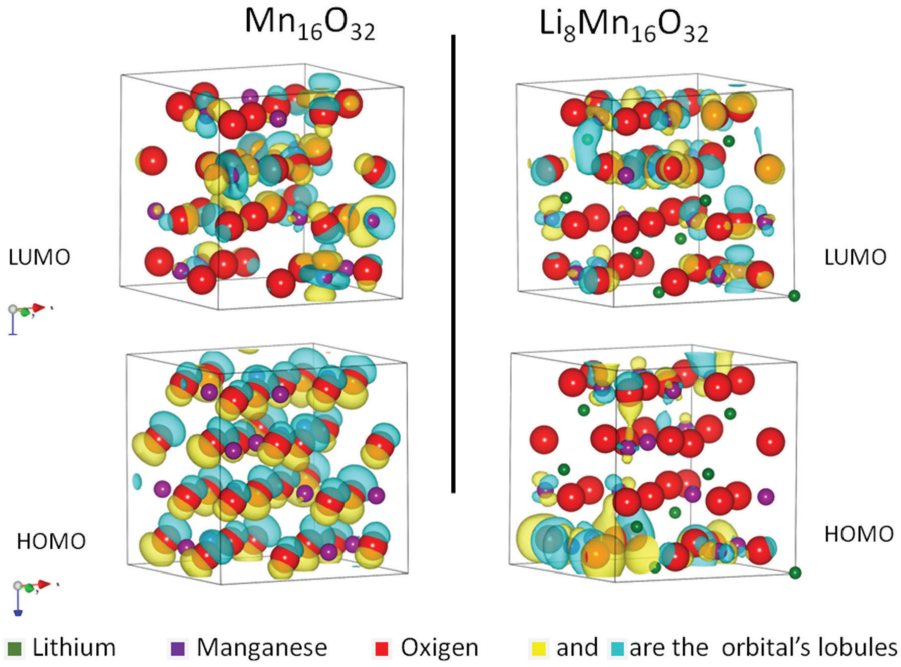

Figure 9. Representation of the frontier orbitals: HOMO and LUMO in optimized structure of MnO_2 and $LiMn_2O_4$.

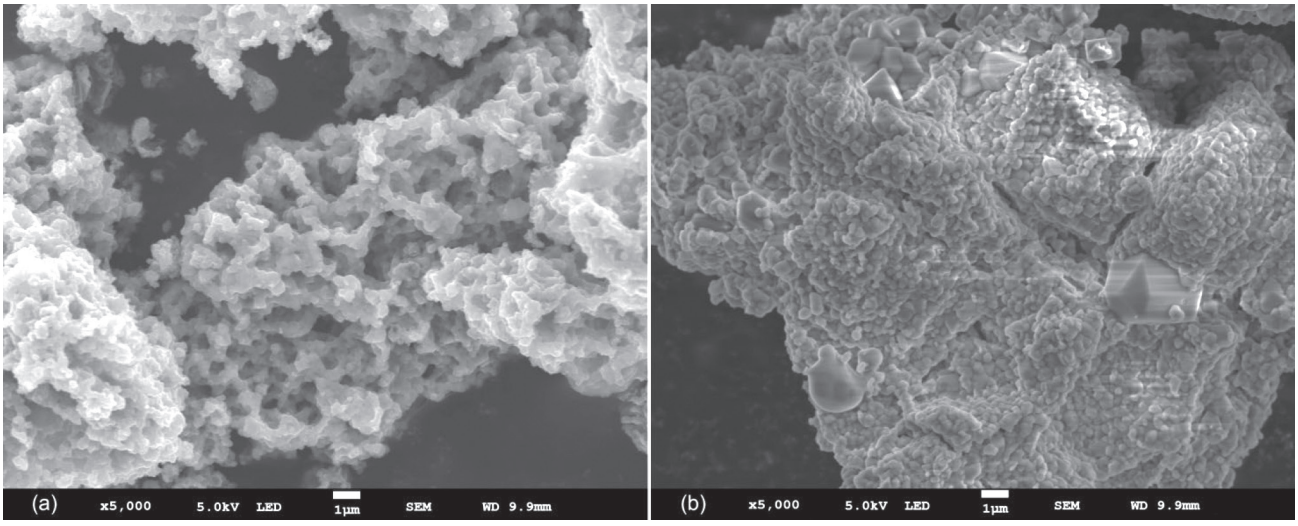

Figure 10. SEM images of $LiMn_2O_4$ treated at: (a) 500 and (b) 700 °C.

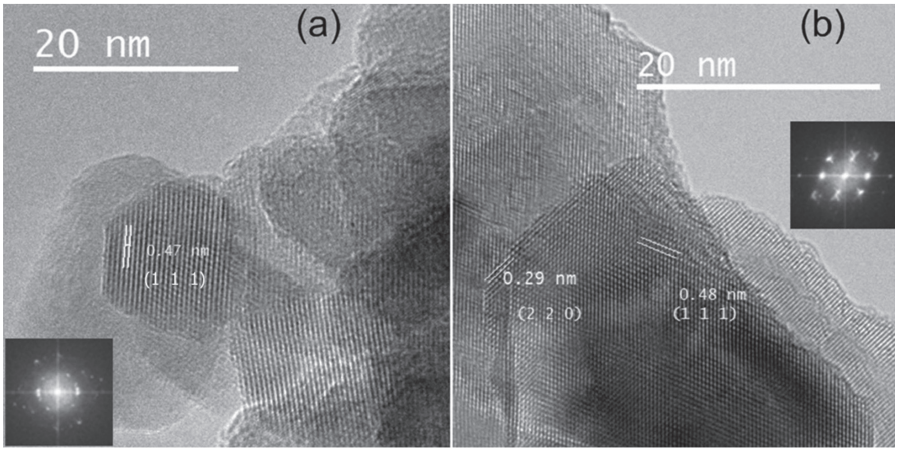

Figure 11. TEM images of $LiMn_2O_4$ treated at (a) 500 and (b) 700 °C. Insert: fast-Fourier transform showing the spinel structure.

In the sample obtained at 700 °C it was possible to estimate distances of 0.48 and 0.29 nm. Those values are related to the index (111) and (220), respectively (values very similar to those obtained by X-ray diffraction).[59] Regarding the average particle size estimated from the TEM analysis for sample treated at 700 °C, it is 25 nm and the particle size distribution is shown in Figure S11 of the Supplementary Information. The average particle size estimated from the TEM analysis is not in agreement with the average crystallite size estimated from XRPD analysis for the sample treated at 700 °C probably due to the negligence of microstrain data. The sample treated at 500 °C is not monodispersed and presents a lot of agglomeration.

Electrochemical measurements

The first twenty two cyclic voltammograms of the samples thermal treated at 500 and 700 °C at a scan rate of 5 mV s^{-1} in the voltage range −0.2 to 1.35 V *vs*. silver as pseudo-reference electrode are shown in Figures 12a and 12b, respectively. The use of the silver pseudo reference electrode generates a decrease of approximately 3 V in the expected potential for the oxidation and reduction peaks, when compared to $Li|Li^+$ electrodes. The profile of voltammograms for both samples implies in reversible process.

The two anodic peaks of the sample thermal treated at 500 °C are in agreement with the data reported in the literature[15,60,61] for $LiMn_2O_4$ at about 0.75 and 0.85 V (3.74 and 3.85 V *vs*. $Li|Li^+$). These two peaks are related to the oxidation process of manganese ion (Mn^{3+}/Mn^{4+}) and lithium ions extraction. In our cyclic voltammogram the first peak of anodic current is observed in approximately 0.8 V and the second in 1.0 V. These two peaks are from the extraction of Li^+ from distinct tetrahedral environments present in the spinel structure. The first peak is related with the extraction of Li^+ ions from a tetrahedral position where

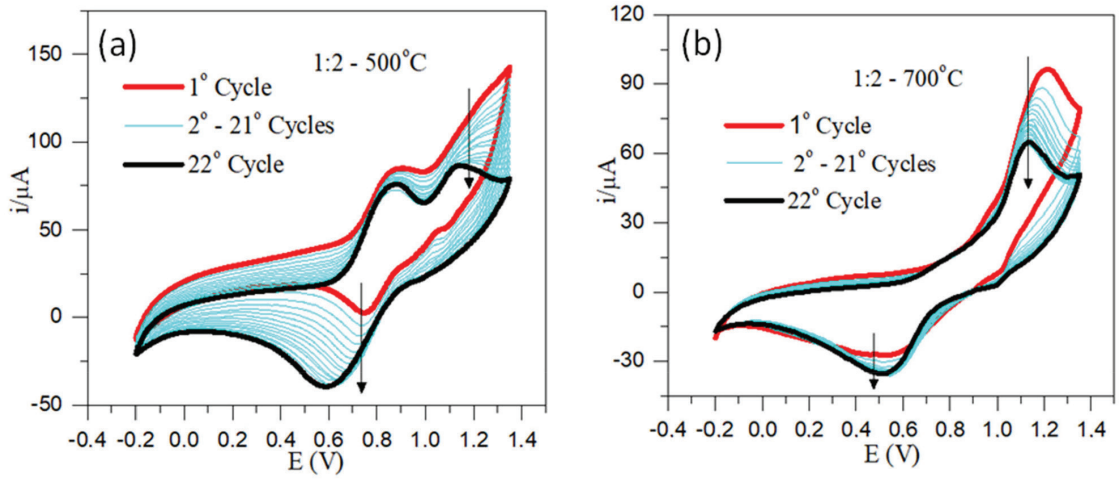

Figure 12. Samples cyclic voltammogram: (a) 500 and (b) 700 °C. Scanning speed of 5 mV s^{-1}.

a repulsive interaction among the lithium ions is observed. The second peak is related with a tetrahedral position where this interaction is not observed.

In the cathodic scan, which represents the reduction of the manganese ions and the concomitant insertion of lithium ions, only one peak was observed for both samples and refers to the lithium ions insertion processes.[62] The observation of only one peak can be attributed to polarization effects.[63,64] In the sample thermal treated at 700 °C, the difference between the insertion/extraction peaks is larger, indicating a great polarization effect in this sample.

The differences between the voltammograms of the two samples mean that the kinetic properties of lithium ion diffusion for the sample thermal treated at 500 °C are better than for the sample thermal treated at 700 °C. These results are correlated to the crystallite size, structural order and Mn^{3+}/Mn^{4+} ratio, structural and morphological differences observed for these two samples as exhibited in XRPD, SEM and TEM data. The particle size and microstructure infer a better charge capacity of the sample treated at 500 °C in relation to the sample treated at 700 °C because the sample at 500 °C presents pores and less sintering (greater surface area), thus facilitating the interface process associated with lithium diffusion.[58,59,65]

It should be noted that recent works[13,58,59] report the importance of the preparation of $LiMn_2O_4$ with specific morphologies, such as high porosity. In these works, the preparations involve several steps to obtain materials with the desired properties. In our case, with only three steps it was possible to obtain a material with very interesting microstructure and porosity, resulting in a significant effect on the electrochemical behavior. However, further experiments are needed to determine if the times used in the heat treatment can be decreased as they are relatively high.

Conclusions

The solution combustion method using corn starch as fuel allows formation of $LiMn_2O_4$ spinel. The crystallite synthesized at the 500 °C thermal treatment is heterogeneous with a large variation size, depending on the analyzed crystallographic plane. At 700 °C, the obtained crystallite was homogeneous with substantially the same crystallite size for all the crystallographic planes. At 700 °C, the peaks were narrower and more defined, due to a more ordering of the crystal. The analyses by SEM and TEM show a porous microstructure composed of nano-sized crystallites for the sample treated at 500 °C. The voltammogram for the sample treated at 500 °C indicates the presence of two characteristic peaks of $LiMn_2O_4$, even at a high scanning speed of 5 mV s^{-1}. These results are in agreement with the theoretical model, indicating the presence of two oxidation states to Mn in the formed spinel (Mn^{3+}/Mn^{4+}) in an antiferromagnetic arrangement with the influence of JT distortion. In this model, the lithium ion removal process was followed by the volume contraction and it was possible to evaluate the Mn^{3+} ions participation in the border region between the valence and conduction bands, which should show the band gap variation during the oxidation processes of those systems.

Supplementary Information

Supplementary data (Williamson-Hall plotting, DOS, orbitals and histograms of SEM and TEM) are available free of charge at http://jbcs.sbq.org.br as PDF file.

Acknowledgments

The authors would like to thank UFF/Proppi, FAPERJ, CAPES and CNPq for financial support, LAME-UFF and

LDRX-UFF for analyzes. The authors would like to thank also LAMAR/CAIPE and Prof Dr Yutao Xing for SEM and TEM images. J. M. S. Jr. and J. A. L. C. R. are thankful for the Brazilian National Laboratory of Synchrotron Light (LNLS), project number: D10B-XPD-9340 for the use of its beam line.

References

1. Schipper, F.; Nayak, P. K.; Erickson, E. M.; Amalraj, S. F.; Srur-Lavi, O.; Penki, T. R.; Talianker, M.; Grinblat, J.; Sclar, H.; Breuer, O.; Julien, C. M.; Munichandraiah, N.; Kovacheva, D.; Dixit, M.; Major, D. T.; Markovsky, B.; Aurbach, D.; *Inorganics* **2017**, *5*, 32.
2. Etacheri, V.; Marom, R.; Elazari, R.; Salitra, G.; Aurbach, D.; *Energy Environ. Sci.* **2011**, *4*, 3243.
3. Goodenough, J. B.; Park, K.-S.; *J. Am. Chem. Soc.* **2013**, *135*, 1167.
4. Manthiram, A.; *J. Phys. Chem. Lett.* **2011**, *2*, 176.
5. Armand, M.; Tarascon, J.-M.; *Nature* **2008**, *451*, 652.
6. Erickson, E. M.; Ghanty, C.; Aurbach, D.; *J. Phys. Chem. Lett.* **2014**, *5*, 3313.
7. YiDi, Z.; Yi, L.; XinHui, X.; XiuLi, W.; ChangDong, G.; JiangPing, Y.; *Sci. China Tech. Sci.* **2015**, *58*, 1809.
8. Yan, J. H.; Liu, X. B.; Li, B. Y.; *RSC Adv.* **2014**, *4*, 63268.
9. Nayak, P. K.; Grinblat, J.; Levi, E.; Markovsky, B.; Aurbach, D.; *J. Power Sources* **2016**, *318*, 9.
10. Freitas, B. G. A.; Siqueira Jr., J. M.; da Costa, L. M.; Ferreira, G. B.; Resende, J. A. L. C.; *J. Braz. Chem. Soc.* **2017**, *28*, 2254.
11. Tarascon, J. M.; Wang, E.; Shokoohi, F. K.; McKinnon, W. R.; Colson, S.; *J. Electrochem. Soc.* **1991**, *138*, 2859.
12. Feng, Q.; Kanoh, H.; Ooi, K.; *J. Mater. Chem.* **1999**, *9*, 319.
13. Zhou, S.; Mei, T.; Wang, X.; Qian, Y.; *Nanoscale* **2018**, *10*, 17435.
14. Xia, Y.; Zhou, Y.; Yoshio, M.; *J. Electrochem. Soc.* **1997**, *144*, 2593.
15. Xia, Y.; Yoshio, M.; *J. Electrochem. Soc.* **1996**, *143*, 825.
16. Rodríguez, R. A.; Pérez-Cappe, E. L.; Laffita, Y. M.; Ardanza, A. C.; Salazar, J. S.; Santos, M. A.; Frutis, M. A. A.; Mohalem, N. D. S.; Alves, O. L.; *Solid State Ionics* **2018**, *324*, 77.
17. Hon, Y. M.; Fung, K. Z.; Hon, M. H.; *J. Eur. Ceram. Soc.* **2001**, *21*, 515.
18. Ishizawa, N.; Tateishi, K.; *J. Ceram. Soc. Jpn.* **2009**, *117*, 6.
19. Whittingham, M. S.; *Chem. Rev.* **2004**, *104*, 4271.
20. Cai, Y.; Huang, Y.; Wang, X. C.; Jian, D.; Tang, X.; *Ceram. Int.* **2014**, *40*, 14039.
21. Naghash, A. R.; Lee, J. Y.; *J. Power Sources* **2000**, *85*, 284.
22. Luo, X. D.; Yin, Y. Z.; Yuan, M.; Zeng, W.; Lin, G.; Huang, B.; Li, Y. W.; Xiao, S. H.; *RSC Adv.* **2018**, *8*, 877.
23. Hashem, A. M.; Abdel-Ghany, A. E.; Abuzeid, H. M.; El-Tawil, R. S.; Indris, S.; Ehrenberg, H.; Mauger, A.; Julien, C. M.; *J. Alloys Compd.* **2018**, *737*, 758.
24. Maino, G.; Carleer, R.; Bonneux, G.; Hardy, A.; Van Bael, M. K.; *Dalton Trans.* **2017**, *46*, 14934.
25. Cao, J.; Guo, S.; Yan, R.; Zhang, C.; Guo, J.; Zheng, P.; *J. Alloys Compd.* **2018**, *741*, 1.
26. Xu, C.; Li, Y.; Xu, H.; Li, P.; Kong, L.; Su, Q.; Cao, X.; *Int. J. Electrochem. Sci.* **2017**, *12*, 5185.
27. Masquelier, C.; Tabuchi, M.; Ado, K.; Kanno, R.; Kobayashi, Y.; Maki, Y.; Nakamura, O.; Goodenough, J. B.; *J. Solid State Chem.* **1996**, *123*, 255.
28. Birke, P.; Salam, F.; Döring, S.; Weppner, W.; *Solid State Ionics* **1999**, *118*, 149.
29. Liu, Z.; Yu, A.; Lee, J. Y.; *J. Power Sources* **1998**, *74*, 228.
30. Shen, C. H.; Liu, R. S.; Gundakaram, R.; Chen, J. M.; Huang, S. M.; Chen, J. S.; Wang, C. M.; *J. Power Sources* **2001**, *102*, 21.
31. Guo, H.; Li, X.; Wang, Z.; Peng, W.; Cao, X.; Li, H.; *J. Power Sources* **2009**, *189*, 95.
32. Liu, J.; Li, G.; Bai, H.; Shao, M.; Su, C.; Guo, J.; Liu, X.; Bai, W.; *Solid State Ionics* **2017**, *307*, 79.
33. Liu, J.; Li, G.; Yu, Y.; Bai, H.; Shao, M.; Guo, J.; Su, C.; Liu, X.; Bai, W.; *J. Alloys Compd.* **2017**, *728*, 1315.
34. Kalyani, P.; Kalaiselvi, N.; Muniyandi, N.; *J. Power Sources* **2002**, *111*, 232.
35. Toby, B. H.; *J. Appl. Crystallogr.* **2001**, *34*, 210.
36. Cusker, L. B.; Von Dreele, R. B.; Cox, D. E.; Louer, D.; Scardi, P.; *J. Appl. Crystallogr.* **1999**, *32*, 36.
37. James, R. W.; *The Crystalline State*, vol. II; Bragg, L., ed.; Bradford and Dickens: London, Great Britain, 1962.
38. Stephens, P. W.; *J. Appl. Crystallogr.* **1999**, *32*, 281.
39. Williamson, G. K.; Hall, W. H.; *Acta Metall.* **1953**, *1*, 22.
40. Ponzio, E. A.; Benedetti, T. M.; Torresi, R. M.; *Electrochim. Acta* **2007**, *52*, 4419.
41. Guidon, M.; Hutter, J.; VandeVondele, J.; *J. Chem. Theory Comput.* **2010**, *6*, 2348.
42. Perdew, J. P.; Ruzsinszky, A.; Csonka, G. I.; Vydrov, O. A.; Scuseria, G. E.; Constantin, L. A.; Zhou, X.; Burke, K.; *Phys. Rev. Lett.* **2008**, *100*, 136406.
43. The CP2K Developers Group; *CP2K Open Source Molecular Dynamics Program*, version 5.1.0; CP2K Foundation, Switzerland, 2017. Available at http://www.CP2K.org, accessed in January 2018.
44. Braga, T. P.; Dias, D. F.; Sousa, M. F.; Soares, J. M.; Sasaki, J. M.; *J. Alloys Compd.* **2015**, *622*, 408.
45. Silva, S. P.; Silva, P. R. C.; Urbano, A.; Scarminio, J.; *Quim. Nova* **2016**, *39*, 901.
46. Antolini, E.; *Solid State Ionics* **2004**, *170*, 159.
47. Brinker, C. J.; Scherer, G. W.; *The Physics and Chemistry of Sol-Gel Processing*; Academic Press Inc.: San Diego, USA, 1990.

48. Vande, V. J.; Krack, M.; Mohamed, F.; Parrinello, M.; Chassaing, T.; Hutter, J.; *Comput. Phys. Commun.* **2005**, *167*, 103.
49. Blochl, P. E.; *Phys. Rev. B* **1994**, *50*, 17953.
50. Blochl, P. E.; Forst, C. J.; Schimpl, J.; *Bull. Mater. Sci.* **2003**, *26*, 33.
51. Visinescu, D.; Tirsoaga, A.; Patrinoiu, G.; Tudose, M.; Paraschiv, C.; Ianculescu, A.; Carp, O.; *Rev. Roum. Chim.* **2010**, *55*, 1017.
52. Tirsoaga, A.; Visinescu, D.; Jurca, B.; Ianculescu, A.; Carp, O.; *J. Nanopart. Res.* **2011**, *13*, 6397.
53. Bianchini, M.; Suard, E.; Croguennec, L.; Masquelier, C.; *J. Phys. Chem. C* **2014**, *118*, 25947.
54. Gonçalves, N. S.; Carvalho, J. A.; Lima, Z. M.; Sasaki, J. M.; *Mater. Lett.* **2012**, *72*, 36.
55. Maniammal, K.; Madhu, G.; Biju, V.; *Phys. E* **2017**, *85*, 214.
56. Yi, T.-F.; Hao, C.-L.; Yue, C.-B.; Zhu, H.-S.; Shu, J.; *Synth. Met.* **2009**, *159*, 1255.
57. Fey, G. T.; Cho, Y.; Kumar, T. P.; *Mater. Chem. Phys.* **2004**, *87*, 275.
58. Chen, J.; Zhao, N.; Zhao, J.; Li, J.; Guo, F.-F.; Li, G.-D.; *J. Solid State Electrochem.* **2018**, *22*, 331.
59. Wu, Y.; Cao, C.; Zhang, J.; Wang, L.; Ma, X.; Xu, X.; *ACS Appl. Mater. Interfaces* **2016**, *8*, 19567.
60. Iqbal, A.; Iqbal, Y.; Khan, A. M.; Ahmed, S.; *J. Saudi Chem. Soc.* **2018**, *22*, 449.
61. Li, X.; Shao, Z.; Liu, K.; Liu, G.; Xu, B.; *J. Electroanal. Chem.* **2018**, *818*, 204.
62. Ouyang, C. Y.; Shi, S. Q.; Lei, M. S.; *J. Alloys Compd.* **2009**, *474*, 370.
63. Xu, W.; Bai, H.; Li, Q.; Feng, T.; Guo, J.; Feng, L.; Su, C. W.; Bai, W.; Liu, X.; *Int. J. Electrochem. Sci.* **2017**, *12*, 9758.
64. Lesel, B. K.; Cook, J. B.; Yan, Y.; Lin, T. C.; Tolbert, S. H.; *ACS Energy Lett.* **2017**, *2*, 2293.
65. Chen, J.; Zhao, N.; Li, G.-D.; Guo, F.-F.; Wang, X.; Jia, T., Zhao, J.; Zhao, Y.; Wang, X.; Wan, L.; *Mater. Chem. Phys.* **2016**, *180*, 244.

Submitted: April 29, 2019
Published online: August 14, 2019